

## Heat capacity of nanocrystalline $\text{Yb}_2\text{O}_3$

D. P. Rojas<sup>1,\*</sup>, J. I. Espeso<sup>2</sup>, L. Rodríguez Fernández<sup>3</sup>, L. Fernández Barquín<sup>2</sup>

<sup>1</sup> Dpto. de Estructuras y Física de Edificación. ETSAM. Universidad Politécnica de Madrid. Madrid 28040, Spain.

<sup>2</sup> Dpto. CITIMAC. Facultad de Ciencias. Universidad de Cantabria. Santander 39005, Spain.

<sup>3</sup> SERMET-SCTI, Universidad de Cantabria. Santander 39005, Spain

\*Corresponding author. Email address: [d.rojas@upm.es](mailto:d.rojas@upm.es)

### Abstract

A study of the structural, Raman scattering and thermodynamic properties of a nanocrystalline ceramic rare earth oxide  $\text{Yb}_2\text{O}_3$  and its bulk counterpart is reported. The nanosized sample was obtained by mechanical milling of bulk  $\text{Yb}_2\text{O}_3$  (99.998%, high purity powder). The Rietveld analysis of the X-ray diffraction data indicates the presence of nanoparticles with a mean grain size of  $12 \pm 1$  nm after 75 h of milling time. The crystallographic structure within nanoparticles is cubic  $Ia-3$  and the lattice parameter  $a = 10.455 \pm 0.002$  Å. The nanocrystalline structure is confirmed by the evaluation of transmission electron microscopy images, showing a size distribution with a mean size  $D_{TEM} = 8 \pm 2$  nm. Measurements of the specific heat (2 K to 300 K) reveal an excess contribution respect to the unmilled (bulk) compound in the high temperature region above 70 K. At lower temperatures the results are consistent with a drastic change of the antiferromagnetic contribution (ordered below  $T_N = 2.2$  K) as a result of the magnetic disorder arising from the size reduction process. The specific heat above  $T_N$  for the bulk and nanocrystalline samples are explained by the interplay among the phonon contribution, crystalline field and the presence of anharmonic effects. In the nanocrystalline state, broadening and shifts of the contribution of phonon modes to the Raman spectra, and a further reinforcement of the anharmonic contribution are found.

*Keywords:* A: Milling; B: X-ray methods; Electron microscopy; C: Thermal properties; D: Yb<sub>2</sub>O<sub>3</sub>

## **1- Introduction.**

Rare earth oxides belong to a large class of materials displaying very attractive physical properties, with a high thermal stability, suitable for a variety of applications [1,2]. Among those compounds, the ceramic oxide Yb<sub>2</sub>O<sub>3</sub>, also known as “Ytterbia”, has widely been used in materials science research [3]. The material is used in high temperature (larger than 1500 °C) sensors measuring the radiation from the transition of 4*f* electrons in the Yb<sup>3+</sup> ions due to thermal excitation [4]. Another application is their capability as an efficient sintering additive for the improvement of the mechanical properties and thermal conductivity of ceramics [5]. Moreover, they have also been applied as doped ZrO<sub>2</sub>-based composite electrolyte materials, showing high conductivities, essential in the development of intermediate temperature fuel cells [6].

Over last years, the “burst” of nanotechnology research has promoted the use of Yb<sub>2</sub>O<sub>3</sub> in nanosized form and widen the possibilities of its potential applications. There are some fine examples: nano-Yb<sub>2</sub>O<sub>3</sub> compounds are valuable to optimize the sintering performance of quartz ceramic materials [7] and in the development of optoelectronic devices, improving the optical data manipulation [8]. In the area of agriculture, they are employed in the fabrication of biosensors for urea (extensively used as fertilizers) detection in water [9]. In the ample biomedical field research, multiple assays have demonstrated the excellent biocompatibility of prepared Gd<sup>3+</sup>-doped Yb<sub>2</sub>O<sub>3</sub> nanoparticles for *in vivo* applications [10].

Since the effect of nano-Yb<sub>2</sub>O<sub>3</sub> addition on the properties of the materials may depend on the size or shape of the nanomaterial, several methods have been employed for the preparation of this ceramic oxide in nanometric form. For instance, the electrospinning technique [11] and the hydrothermal method [12] are adequate. In the latter, nanometric Yb<sub>2</sub>O<sub>3</sub> has been synthesized successfully as nanowires, nanorods and nano-square plates.

To achieve further technical potential, it is crucial to understand the effect of the reduction of the size of the samples on the different physical properties of this material itself. In this sense, the present work will move forward in such a direction providing a deeper insight in the thermal properties, namely the heat capacity. Considering our previous experience in the preparation of rare earth-based nanoparticles, in particular, Yb alloys [13,14], and other rare earths [15, 16], we have selected the mechanical milling procedure to obtain the nanometric sample for the present work. This technique is suitable to obtain large (and cost-effective) quantities of nanocrystalline materials and the size can be tuned in a controlled way, with a reasonable size distribution. To achieve a complete understanding, of the specific heat from 2 K to 300 K, we are discussing results obtained in compounds at the nanoscale together with those corresponding to bulk  $\text{Yb}_2\text{O}_3$ .

## **2- Experimental details**

Nanocrystalline  $\text{Yb}_2\text{O}_3$  was prepared by high-energy mechanical milling of a starting commercial (high purity, 99.998 %) powder from Alfa-Aesar company. The powder was milled in a planetary ball system (Retsch PM 400/2) at a rotation speed of 200 rpm, using containers and balls made of tungsten carbide. These containers are thoroughly cleaned, including a grinding process with Si. The structural characterization was carried out in a Bruker D8 Advance diffractometer, with  $\text{Cu-K}_\alpha$  radiation ( $\lambda = 1.5418 \text{ \AA}$ ). Transmission electron microscopy (TEM) was performed in a JEOL JEM 1100 microscope at an operating voltage of 80 kV. For the TEM characterization, the pressed pellet sample was first grinded with an agate mortar, and later dispersed in ethanol and ultrasonicated in a water bath for several hours at room temperature. A drop of the nanoparticle suspension was placed onto a 300 mesh carbon-coated Cu grid, and air-dried before TEM observation. Heat capacity data as a function of temperature were collected in a Quantum Design PPMS device in the temperature range from 2 K to 300 K. For this measurement, the powder was pressed in a press pellet die, and then a slice ( $2.5 \times 2.5 \text{ mm}^2$ , 14 mg, approximately) was cut. Afterwards, it was attached to the sample holder platform with a standard cryogenic grease to ensure good thermal contact. Raman spectra were

collected at room temperature using the 514 nm line of a Coherent Innova 70 (Ar + Kr) laser with a triple monochromator Horiba-Jobin-Yvon T64000 spectrometer in subtractive mode with backscattering configuration, equipped with a Horiba Symphony liquid-nitrogen-cooled CCD detector. The laser line was focused on the sample with a 20X objective, and the powder was kept below 2 mW to avoid heating effects. The laser spot was 20 mm in diameter and the spectral resolution was better than  $0.6 \text{ cm}^{-1}$ .

### 3- Results and Discussion

#### 3.1- X-ray diffraction.

The X-ray diffractograms and the Rietveld refinement of the bulk (henceforth referred as 0 h or unmilled sample) and 75 h milled  $\text{Yb}_2\text{O}_3$  are presented in Figure 1. A reduction of the intensity and broadening of the peaks for the milled sample are observed. This is connected to the characteristic of reduction of the size of the particles and increase of the lattice microstrain [13-16]. The crystallographic structure of the cubic stable  $\text{Yb}_2\text{O}_3$  phase is a primitive cell containing 16 formula units with 32 Yb atoms distributed among the two inequivalent positions at  $8b$  and  $24d$  sites, and 48 oxygen atoms (O) at the  $48e$  site [1]. The Rietveld refinements of both unmilled and 75 h milled samples are consistent with a single cubic phase  $Ia-3$ - type (206) space group. For the unmilled  $\text{Yb}_2\text{O}_3$ , the value of the lattice parameter is  $a = 10.437 \pm 0.002 \text{ \AA}$  in good agreement with the previously reported value [1]. The refinement is excellent with a very low Bragg factor ( $R_{\text{Bragg}} = 3.6 \%$ ). In the nanometric sample additional microstructure parameters to extract the nanoparticle size ( $D_{\text{XRD}}$ ) and microstrain ( $\varepsilon$ ) were considered. Although a Williamson–Hall analysis can be carried out to extract both parameters, it is most complete to perform a profile-fitting procedure of the diffraction peaks using the Rietveld method [15, 17]. The result of the fitting gives  $a = 10.455 \pm 0.002 \text{ \AA}$ , for the lattice parameter,  $D_{\text{XRD}} = 12 \pm 1 \text{ nm}$  for the mean size of the particles, and  $\varepsilon = 0.21 \pm 0.02 \%$  for the microstrain. The refinement shows a good

reliability (as for the bulk case), with a Bragg factor below 10 % ( $R_{\text{Bragg}} = 8.8\%$ ). Hence, the milling route allows producing nanometric powder of  $\text{Yb}_2\text{O}_3$  in large quantities easily.

### 3.2- Transmission electron microscopy.

The structural characterization was completed using the transmission electron microscopy (TEM) to extract the mean nanoparticle size and the size distribution [18]. Figure 2 shows a selected image obtained for the 75 h milled  $\text{Yb}_2\text{O}_3$  sample, with several representative nanoparticles showcasing a mean size  $D_{\text{TEM}} = 8 \pm 2$  nm. This mean value was obtained from the analysis of the size-distribution histogram, following the usual Log-normal function. This value of the mean particle size is near to that calculated by Rietveld refinement of the XRD pattern. It has been impossible to ascertain better the lower size histograms with the images at hand. It appears that the milling process reaches a limiting low value of the size around 5 nm, at least with the planetary system here employed, as obtained for instance, in other materials [15,19-21]. In any case, the shape of the size distribution is reasonable and the value of the mean particle size is close to that calculated by Rietveld refinement of the XRD pattern. This is the relevant finding for the rest of the specific heat study: an ensemble of nanocrystalline (*Ia-3*) particles of  $\text{Yb}_2\text{O}_3$  is obtained.

### 3.3- Specific heat.

The thermal behavior is mainly governed by the phonon (lattice vibrations) contribution, which should be influenced by grain size reduction and/or disorder effects [19-21]. In the present work, measurements and a detailed analysis of the specific heat of the unmilled and 75 h milled (12 nm)  $\text{Yb}_2\text{O}_3$  samples are provided. Figure 3 shows the temperature dependence of the (pressure constant) specific heat ( $c_p$ ) of both samples, between 2 K to 300 K. From room temperature ( $c_p \approx 120$  J/molK) to low temperatures, a

conventional decrease of  $c_p$  is observed down to around 10 K. For  $T < 10$  K, an increase of the specific heat is observed, especially for the unmilled  $\text{Yb}_2\text{O}_3$  ( $\approx 20$  J/molK). From these measurements, it turns out the existence of an excess  $c_p$  contribution in the 75 h milled sample respect to the one corresponding to the unmilled (0 h) compound for  $T > 70$  K. Below this temperature, the previous tendency changes resulting in a higher contribution for the unmilled sample, as detailed in the inset of Figure 3. The overall behavior of the curves can be explained by the combined influence of the reduction in the antiferromagnetic contribution at low temperatures (in the 75 h milled sample), and the variations in the phonon spectra, as will be discussed below.

The magnetic contribution to the specific heat should also be appearing for  $T < T_N$ . The effect of the size reduction process on the magnetic contribution of the specific heat of  $\text{Yb}_2\text{O}_3$  is revealed in Figure 4, where we now concentrate on  $T \leq 10$  K. It is worth mentioning that previous studies on the specific heat of  $\text{Yb}_2\text{O}_3$  were limited to the temperature range above 10 K [22]. A distinct peak in the 0 h sample is evident, which is associated to the antiferromagnetic transition at  $T_N = 2.2$  K. Such an antiferromagnetic state was established in detail for  $\text{Yb}_2\text{O}_3$  by neutron diffraction experiments in a previous work [23]. The magnitude of the magnetic peak of the unmilled sample is reduced four times for 75 h sample. This reduction has been observed in other rare earth-based magnetic systems, where the magnetic  $c_p$  peak can even disappear. The origin is related to finite-size, surface and disorder effects in nanoparticle systems [19, 20]. Above  $T_N$ , magnetic short-range magnetic correlations are observed, until 7 K in the unmilled and to 9 K in the milled sample. The inset of Figure 4, shows details of the magnetic contribution in the milled sample. The single peak (lambda anomaly), typical contribution in the unmilled  $\text{Yb}_2\text{O}_3$  changes to a more complex magnetic  $c_p$  contribution when the material is formed by an ensemble of nanoparticles. This effect is subtle and

cannot be further discussed with the current data. In fact, this effect is reflected in the magnetic contribution of the milled Yb alloys at low temperatures, as in the intermediate valence YbAl<sub>3</sub> [13]. It also emphasizes the importance of the characterization of nanosized Yb<sub>2</sub>O<sub>3</sub> in the study of nanometric Yb strongly correlated electron materials [13, 14, 24]. In particular, in the milled YbAl<sub>3</sub> the impurity contribution of the Yb<sub>2</sub>O<sub>3</sub> oxide can be unveiled by subtracting the electronic and phonon contributions ( $c \approx \gamma T + \beta T^3$ ) [13], from the total specific heat at low temperatures. This equally results in a double-peaked shape for the magnetic contribution associated to Yb<sub>2</sub>O<sub>3</sub>, similar to the obtained here for Yb<sub>2</sub>O<sub>3</sub> (Figure 4).

From 10 K up to room temperature, the pure magnetic effects are negligible. In such a temperature range, two additive contributions are expected, which are stemming from the crystal field and the crystal lattice vibrations. Due to the insulator nature of ceramic oxide Yb<sub>2</sub>O<sub>3</sub> the linear electronic term ( $\gamma T$ , where  $\gamma$  is the Sommerfeld coefficient) typical for metals, will not be considered. Let us start with the Schottky type contribution of CF levels to the specific heat [23, 25]. In magnetic Yb<sub>2</sub>O<sub>3</sub> oxide, the Yb atoms are in Yb<sup>3+</sup> valence state, as corroborated from the analysis of XANES (X-ray Near Edge Structure) measurements [13]. This valence state is even maintained when milling Yb<sub>2</sub>O<sub>3</sub> up to 75 h (12 nm), similar to what occurs in magnetic 30 h milled YbNi<sub>2</sub> nanometric alloys (10 nm) [14]. Thus, this state is consequent with its magnetic behavior as well. Therefore, the eight-fold degenerate ground term of Yb<sup>3+</sup> with  $J = 7/2$  should be split into two doublets and one quartet in cubic symmetry [26]. However, there may be cases where the local symmetry around the magnetic ions may differ slightly from the cubic symmetry. Thus, smaller terms of lower symmetry must be considered and, the quartet state could additionally split into two doublets. Hence, the final configuration includes four doublets for the CF states of Yb<sup>3+</sup>. This is the case of

Yb<sub>2</sub>O<sub>3</sub> oxide with two Yb atoms at different positions (8b and 24d) within the crystallographic structure of the *Ia-3*-type and different coordination with the oxygen atoms [23]. In fact, a detailed analysis of the specific heat experimental data of Yb<sub>2</sub>O<sub>3</sub> indicates that the levels scheme with four doublets is more adequate to describe the contribution from the CF levels [22, 25]. From these reports, the values of the splitting of the different doublets for the two Yb atoms at positions 8b (*C<sub>3i</sub>*) sites and 24d (*C<sub>2</sub>*) sites were estimated. Their analysis indicates the existence of a ground state doublet, with approximate near positions for the excited doublets centered around 515 K (361 cm<sup>-1</sup>), at 954 K (668 cm<sup>-1</sup>) for the second and with overall splitting of 1429 K (1000 cm<sup>-1</sup>) for the two Yb positions [25], taking the equivalence between the units (1 K ≈ 0.7 cm<sup>-1</sup>).

The second additive contribution to the total specific heat is that associated to the phonon modes [27]. This contribution commonly referred as “lattice specific heat”, is well described within the Debye model, and associated to the existence of acoustic phonon modes of vibrations. According to previous sonic experiments in bulk Yb<sub>2</sub>O<sub>3</sub>, a value of the Debye temperature  $\theta_D = 385$  K was estimated from the Young's and shear moduli [28]. In a first approximation of the analysis of the specific heat of the unmilled Yb<sub>2</sub>O<sub>3</sub> sample, the fit of the experimental data for  $T > 20$  K with a fixed contribution of CF levels (scheme of four doublets [25]), and the phonon contribution with a single

Debye temperature was unsuccessful giving a value of  $\chi^2 = 1989$ . 
$$\chi^2 = \sum_i \left( \frac{y - y_i}{w_i} \right)^2,$$

where  $y$  is the fitted value for a given point,  $y_i$  is the original data value for the point and  $w_i$  is the standard error for the point. To overcome that unreasonable result, peculiarities of the phonon spectra with two different Yb and O atoms and, additionally, with two Yb atoms at different crystallographic positions should be considered. The irreducible

representations of vibrations of atoms occupying the different sites in  $\text{Yb}_2\text{O}_3$  are:  $C_2$  (Yb) ( $A_g + A_u + E_g + E_u + 5T_g + 5T_u$ );  $C_{3i}$  (Yb) ( $A_u + E_u + T_u$ ), and  $C_l$  (O) ( $3A_g + 3E_g + 9T_g$ ), associated to Raman-active ( $A_g$ ,  $E_g$  and  $T_g$  symmetries) and infrared-active ( $A_u$ ,  $E_u$  and  $T_u$  symmetries), respectively [25, 29]. Raman spectroscopy measurements in the unmilled (0 h) and 75 h milled  $\text{Yb}_2\text{O}_3$  are presented in Figures 5 to 7. The main contributions can be focused on three regions. A first group of low frequency peaks appears up to  $145 \text{ cm}^{-1}$  (see Figure 5). A central range lies between  $270 \text{ cm}^{-1}$  and  $400 \text{ cm}^{-1}$  (Figure 6), and a last set of peaks are visible between  $530 \text{ cm}^{-1}$  and  $700 \text{ cm}^{-1}$  (Figure 7). The mode assignment sequence has been performed according to previous Raman scattering studies reported on bulk  $\text{Yb}_2\text{O}_3$  [25], where a shift of the peaks from 2 to  $8 \text{ cm}^{-1}$  of Raman spectra from 10 K to 300 K should be considered. The spectra are dominated by a high intensity peak ( $A_g+T_g$ ), being in the bulk sample around  $361 \text{ cm}^{-1}$  with a shoulder centered at  $336 \text{ cm}^{-1}$ . This last contribution (shoulder) can be ascribed to the Stark level assignment for  $\text{Yb}^{3+}$  ion in  $C_{3i}$  site ( $\Gamma_{el}$ ,  $C_{3i}$ ) [25, 29].

Comparative studies of Raman spectroscopy in a series of cubic oxides of the  $\text{R}_2\text{O}_3$  (R- Rare earth) type suggest that the low frequency peaks (from  $82 \text{ cm}^{-1}$  to  $143 \text{ cm}^{-1}$ ) can be mainly ascribed to the vibration of rare earth ions [31]. Therefore, due to the large difference between the mass of the oxygen and rare earth ions, the phonon modes can be separated into two groups: those of high-frequency mainly related to oxygen vibrations, and the low-frequency ones, with a preference of rare-earth atoms [31].

In view of the findings just described, it seems plausible to consider two phonon contributions involving groups of different atoms. In this sense, in a second approximation to evaluate the different contributions to the specific heat of  $\text{Yb}_2\text{O}_3$  besides de CF contribution [25], we have considered an additional Debye function to take into account the presence of atoms contributing preferentially to the low or high

frequency phonon modes. In the Debye harmonic approximation of the lattice contribution [19, 27], the specific heat at constant volume is given by:

$$c_v^h(N_{at}, \theta_D) = 9N_{at}R \left( \frac{T}{\theta_D} \right)^3 \int_0^{\frac{\theta_D}{T}} \frac{x^4 e^x dx}{(e^x - 1)^2} \quad (1)$$

Where  $N_{at}$  is the number of atoms (for instance,  $N_{at} = 5$  for  $\text{Yb}_2\text{O}_3$ ), and  $\theta_D$  is the Debye temperature. Then, to account for the phonon contribution, we have considered the following function for the fitting:

$$c_{ph} = f \cdot c_v^h(N_{at}, \theta_{D1}) + (1-f) \cdot c_v^h(N_{at}, \theta_{D2}) \quad (2)$$

Where  $f$  is the fraction of the total number of atoms ( $N_{at}$ ), which can be characterized with a Debye temperature  $\theta_{D1}$ . Therefore  $(1-f)$  will be the fraction of the atoms related with the second  $\theta_{D2}$ . According to the Debye model, the characteristic temperature ( $\theta_D$ ) is directly related with the frequency of vibrations ( $h\nu = k\theta_D$ ), where  $h$  and  $k$  are the Planck's and Boltzmann's constants, respectively. The CF contribution has been fixed according to the values of the splitting given in reference [25]. The results of the fitting for  $T > 20$  K indicate that with a fixed parameter  $N_{at} = 5$ , there is a very visible discrepancy above 200 K, with the fitting curve giving lower values respect to the experimental ones, being  $\chi^2 \approx 63$ . Thus, it turns out that an extra (small) contribution should be taken into account.

An important fact to be considered is that the experimental curve is obtained at constant pressure ( $c_p$  vs.  $T$ ), whereas the Debye model is related with a process at constant volume following a harmonic approximation ( $c_v^h$ ). The specific heats at constant pressure and volume are related by the following thermodynamic relation:

$$c_p - c_V = TV_m \alpha_v B_T \quad (3)$$

where  $B_T$ ,  $V_m$  and  $\alpha_v$  are the isothermal bulk modulus, the molar volume, and the volume thermal-expansion coefficient, respectively [32]. There are a lot of solids, for instance pure metals as Fe and Cu, where the difference around room temperature reflected in equation (3) is very small and the specific heat associated to phonons is well described using solely the Debye model [19]. However, in the case of the  $\text{Yb}_2\text{O}_3$ , the difference observed in our fits between the experimental and the theoretical model may be indicative of a non-negligible anharmonic correction at high temperatures as observed in other materials [33, 34]. In fact, temperature dependent Raman scattering studies above 80 K in  $\text{Yb}_2\text{O}_3$  reveal that anharmonic contributions arising from the phonon-phonon interaction due to the lowest-order cubic and quartic terms in the inter-atomic potential affect the phonon modes [29]. This suggests that the anharmonicity effects must be taken into account in  $\text{Yb}_2\text{O}_3$  when analyzing the heat capacity. In this line, these anharmonic effects can be taken into account by a simple phenomenological correction  $c_p = c_V^h(1 + \eta T)$ , which is similar to the well-known relation given by equation (3), but with  $c_V^h$  instead of  $c_V$  [33,34]. Within this framework, our third evaluation of the experimental data has considered anharmonic effects. The CF contribution is fixed according to estimated parameters in [25]. Thus, the total experimental specific heat is a sum of the lattice vibrations with the anharmonic correction and CF contributions ( $c_{CF}$ ):

$$c_p = c_{ph}(1 + \eta T) + c_{CF} \quad (4)$$

The result of the fitting procedure for  $T > 20$  K (solid line), in this third approximation, is shown in Figure 8, in a  $c_p/T$  vs.  $T$  plot. A good agreement with the experimental data

is obtained ( $\chi^2 \approx 9$ ), being the parameters:  $N_{at} = 5$  (fixed value),  $\theta_{D1} = 771 \pm 5$  K,  $\theta_{D2} = 177 \pm 2$  K,  $f = 0.674 \pm 0.004$ , and  $\eta = (1.7 \pm 0.1) \cdot 10^{-4}$  K<sup>-1</sup>. In this approximation, the value of  $\theta_{D1} = 771$  K (540 cm<sup>-1</sup>) would reflect the contribution from high frequency modes, being shifted to the side of the one of main lines in the Raman spectrum around 610 cm<sup>-1</sup>, whereas  $\theta_{D2} = 177$  K (124 cm<sup>-1</sup>) is near to the center of the group of low frequency peaks close to the contribution from the A<sub>g</sub> + T<sub>g</sub> mode located at 118 cm<sup>-1</sup> (169 K) (see Figure 5). Interestingly, the value obtained for the fraction of atoms contributing to the high frequency vibrations ( $f = 0.674$ ) gives a number of atoms  $f \cdot N_{at} = 3.37$  atoms from the total of 5 in Yb<sub>2</sub>O<sub>3</sub>. This finding indicates the *preference* of the oxygen atoms to contribute to high frequency phonon modes. Consequently, the other fraction  $(1-f) \cdot N_{at} = 1.63$  can be associated to the *preference* of Yb to participate in low frequency vibrations. It is worth commenting that this separation into two groups is an approximation since modes of vibrations reflected in the peak centered around 361 cm<sup>-1</sup> (514 K) could contribute equally to the low or high frequency modes in our approximation for the analysis of the specific heat data. Moreover, some of the observed modes in the Raman spectra may be a superposition (closely spaced) different type of modes [29]. Thus, for this reason the word *preference* should be emphasized for this approximation [31]. Concerning the anharmonic correction, the value of the parameter  $\eta = 1.7 \cdot 10^{-4}$  K<sup>-1</sup> is of the same order as that obtained for the series of compounds  $RMIn_5$  ( $R = \text{Gd, La, Y}$ ;  $M = \text{Co, Rh}$ ) [34]. Anharmonic effects are important for  $T > 150$  K, being the correction around 5% at 300 K.

Once we have unambiguously established the contributions to the total specific heat in the unmilled oxide, it is possible to address correctly the variations in the nanosized Yb<sub>2</sub>O<sub>3</sub> (75 h). In this case, the evaluation of the different contributions has been carried out taking into account equations (2) and (4). However, due to the nanometric nature of

the sample, the fraction  $f$  should also account the fraction of atoms contributing to low frequencies due to the softening of phonon modes at the surface of the particles. In materials composed of a single type of atoms, as some nanocrystalline metals for example, there should be a parameter associated to the contribution of the atoms at the surface of the particles [19]. In nanometric  $\text{Yb}_2\text{O}_3$ , the situation is more complex because there exist contributions from rare earth and oxygen atoms to low and/or high frequency modes, as commented above. Thus, it will be more difficult to separate the surface contribution from that stemming from the nanoparticle core. We are explaining below the influence of the reduction in particle size in the lattice, magnetic and CF contributions to the specific heat.

The phonon spectrum of the bulk material is expected to change when reducing the size of the samples because the influence of size and surface effects on the phonon modes [19, 35, 36]. In this sense, Raman scattering measurements in nanosized (12 nm) 75 h milled  $\text{Yb}_2\text{O}_3$  (Figures 5 to 7) show the typical broadening of the peaks and shifts of their positions respect to the unmilled  $\text{Yb}_2\text{O}_3$  due to the nanometric nature of the sample [35, 36]. Low frequency peaks at  $95\text{ cm}^{-1}$  ( $T_g$ ) and  $118\text{ cm}^{-1}$  ( $A_g + T_g$ ) of the unmilled sample are shifted to  $93\text{ cm}^{-1}$  and  $116\text{ cm}^{-1}$ , respectively in the 75 h milled  $\text{Yb}_2\text{O}_3$  (12 nm) (Figure 5). There is also another change in the spectrum respect to the bulk sample, as the peak at  $82\text{ cm}^{-1}$  does not appear and that at  $90\text{ cm}^{-1}$  appears as a broad shoulder of the  $T_g$  mode at  $93\text{ cm}^{-1}$ . On the other hand, the broadening can be clearly observed with the fusion of the peaks at  $137\text{ cm}^{-1}$  ( $T_u$ ) and  $143\text{ cm}^{-1}$  ( $T_u$ ) of the unmilled (0 h) into one broad contribution centered around  $140\text{ cm}^{-1}$  of the 75 h milled  $\text{Yb}_2\text{O}_3$  (Figure 5). As an interesting feature, no contributions are found between  $200\text{ cm}^{-1}$  and  $300\text{ cm}^{-1}$  both in bulk and 75 h milled  $\text{Yb}_2\text{O}_3$  samples (Figure 6). This situation is different to that observed in Raman scattering experiments on  $\text{Ho}_2\text{O}_3$  nanocrystals,

where a new peak arises around  $220\text{ cm}^{-1}$  [37], when compared to the spectrum of the bulk  $\text{Ho}_2\text{O}_3$  [31]. In the highest frequency range (Figure 7), we are focusing on the region from  $530\text{ cm}^{-1}$  to  $650\text{ cm}^{-1}$  (centered around  $610\text{ cm}^{-1}$ ), where the clear contribution from the samples is found. Here, the  $T_u$  mode at  $558\text{ cm}^{-1}$  in the 0 h sample disappears with the milling process, and a shift of the  $T_g$  mode down to  $603\text{ cm}^{-1}$  in the 75 h milled respect to the unmilled (0 h)  $\text{Yb}_2\text{O}_3$  is observed. Additionally, an unidentified broad hump around  $657\text{ cm}^{-1}$  is detected in the milled sample, which is not found in the unmilled (0 h)  $\text{Yb}_2\text{O}_3$ . This last contribution may come from the nanometric nature of the milled sample. In a nanostructured material, it is expected the emergence of new phonon modes associated to phonon confinement and/or to the softening of the phonon modes at the surface of the nanoparticles when reducing the size of the samples [19,35,36]. The experimental observation of these new phonon modes contributions may depend on the size of the particles and the characteristics of the interface of the given nanostructured material [35,36]. Moreover, it has also been observed that the disorder (strain) can also induce the appearance of new phonon modes, as reported for instance in Cr-doped  $\text{PrFeO}_3$  [38]. Thus, according to the features of the contribution found around  $657\text{ cm}^{-1}$  in the 75 h milled  $\text{Yb}_2\text{O}_3$ , this behavior resembles that observed in the Cr-doped  $\text{PrFeO}_3$  system, and probably it could be associated to the increase of the lattice strain during the size reduction (milling) process, as concluded from the analysis of the x-ray diffraction results (Figure 1). In any case, the nature of this contribution may be a subject of future studies of Raman spectroscopy measurements in  $\text{Yb}_2\text{O}_3$  for different milling times, which can elucidate this issue.

Secondly, concerning the magnetic contribution in the milled sample, the “lambda” anomaly in the unmilled  $\text{Yb}_2\text{O}_3$  sample related with the antiferromagnetic order at  $T_N =$

2.2 K is reduced four times after 75 h of milling time (see Figure 4). Consequently, the magnetic contribution associated to CF effects would also be reduced, as has been observed in other Yb milled magnetic systems by the analysis of the experimental data of specific heat and Electron Spin Resonance (ESR) measurements [14]. Thus, it seems plausible to consider a reduction of CF contribution when fitting the specific heat vs. temperature curve of the ensemble of Yb<sub>2</sub>O<sub>3</sub> nanoparticles. This effect was accounted for the fittings leaving free the number of Yb ions, but maintaining a fixed splitting of the CF levels, as obtained from reference [25].

The result of the fitting procedure in Yb<sub>2</sub>O<sub>3</sub> (75 h) is presented in Figure 8 (bottom). In this plot, we have also included the behavior of the main contributions separately to ease the understating: 2 lattice contributions with different Debye temperatures, and the CF. An excellent agreement respect to the experimental data is obtained with a very low  $\chi^2 \approx 3.8$ . The values ( $N_{at} = 5$ , fixed value) of the parameters in the fit give:  $\theta_{D1} = 662 \pm 10$  K,  $\theta_{D2} = 204 \pm 3$  K,  $f = 0.678 \pm 0.009$ ,  $N_{ion} = 1.2 \pm 0.2$  (related to the CF contribution) and  $\eta = (3.6 \pm 0.3) \cdot 10^{-4} \text{ K}^{-1}$ . The value of  $\theta_{D1} = 662$  K ( $463 \text{ cm}^{-1}$ ), as in the unmilled sample, is related with the high frequency modes. It is being shifted practically to the center between the lines at  $366 \text{ cm}^{-1}$  and  $603 \text{ cm}^{-1}$  in the Raman spectrum of the 75 h milled sample. Respect to the low frequency phonons contribution with  $\theta_{D2} = 204$  K ( $143 \text{ cm}^{-1}$ ), this is shifted to higher values respect to that observed in the unmilled sample with  $\theta_{D2} = 177$  K ( $124 \text{ cm}^{-1}$ ), and is near to the contribution of the two modes  $T_u$  centered around  $140 \text{ cm}^{-1}$  of the 75 h milled Yb<sub>2</sub>O<sub>3</sub> (see Figure 5).

Concerning the value obtained for the fraction of atoms contributing to high frequency vibrations ( $f = 0.678$ ), it is close to that obtained for the unmilled sample. In nanocrystalline metals, this value would indicate a fraction  $(1 - f) = 0.32$  of atoms

located at the surface of the nanoparticles using a single model, different to that expected of 0.25 for 12 nm nanoparticles [19]. As commented above, this approximation, which works well for systems made of a single type of atoms, may not be so adequate in  $\text{Yb}_2\text{O}_3$  due to the existence of different atoms contributing to low and/or high frequency phonon modes. Therefore, it is more difficult to reach a proper estimation of the contribution from the core of the nanoparticles. Furthermore, the value obtained for the parameter  $N_{ion} = 1.2$  reflects a reduction of 40 % in the magnetic contribution of the CF effects related with the magnetic disorder.

Regarding the anharmonic correction, the value of the parameter  $\eta = 3.6 \cdot 10^{-4} \text{ K}^{-1}$  increases in comparison to the unmilled sample, being important for  $T > 100 \text{ K}$ , with a correction around 9 % at 300 K, as shown in Figure 5 (bottom). From the result of the fitting it seems that anharmonic effects are reinforced with the process of the size reduction of the sample. This decrease of the size is also accompanied by an increase of the lattice strain ( $\varepsilon = 0.21 \%$ ) as obtained from the Rietveld analysis of the X-ray diffraction data, which indicates the influence of disorder on the anharmonic effects in  $\text{Yb}_2\text{O}_3$ . Indeed, measurements of microstructure, thermal expansion and specific heat of ordered and disordered  $\text{Pd}_3\text{V}$  alloy showed that the 70 % of the difference of the vibrational entropy of disordered and ordered  $\text{Pd}_3\text{V}$  can be attributed to anharmonic effects [39].

#### **4- Conclusions**

The structural state and the specific heat behavior of bulk (unmilled) ceramic oxide  $\text{Yb}_2\text{O}_3$ , and a nanocrystalline sample with mean grain size  $\approx 12 \text{ nm}$  obtained by mechanical milling have been investigated. The specific heat shows a thermal behavior which is dominated by the contribution from the lattice vibrations, with a small low

temperature contribution ( $T < 12$  K) stemming from the onset of antiferromagnetic order at  $T_N = 2.2$  K. Above this temperature, the experimental data have been analyzed in detail, requiring the consideration of contributions from phonons, crystal field and anharmonic effects. According to peculiarities of the phonon spectrum of the series of rare earth  $R_2O_3$  oxides [30, 31], an approximation which takes into account the presence of atoms contributing preferentially to the low (Yb atoms) or high (oxygen atoms) frequency phonon modes has been employed [31]. The validity of this approximation has been checked by the analysis of the parameters given by the fitting procedure. These are consistent with the number of Yb and oxygen atoms in  $Yb_2O_3$ , as well as by the correlation of the other parameters with the observed lines in the measured Raman spectra. In the nanometric sample the phonon spectrum is affected, with a broadening and shifts of the peaks respect to the unmilled sample. In the present work, it has been shown that very fine structural details should be considered to separate the contributions from the core and the surface atoms. This contrasts with previous analyses in simple nanocrystalline metals, in which such a separation was possible [19]. A way to disentangle the core and shell contributions could be to work on systems with several samples (with different nanoparticle sizes), which can constitute a future research line. Finally, the analysis of the experimental data is consistent with the presence of anharmonic effects, which are in agreement with Raman scattering experiments [29]. These are reinforced in the nanometric sample with the increase of disorder (lattice strain).

### **Conflicts of interest**

The authors declare no conflict of interest.

### **Acknowledgments**

This work has been supported by the Spanish MAT2017-83631-C3-R grant. The authors are indebted to J. Alonso from University of Cantabria for his critical review of the manuscript.

## References.

- [1] L. Eyring, in Handbook on the Physics and Chemistry of the Rare Earths, edited by K. A. Gschneidner and L. Eyring (North-Holland, Amsterdam, 1979), Vol. 3, p. 339.
- [2] Gin-ya Adachi, N. Imanaka, The Binary Rare Earth Oxides, Chem. Rev. 98 (1998) 1479-1514, <https://doi.org/10.1021/cr940055h>.
- [3] Aftab, Alina, Sintering Behavior, Structural, and Catalytic Properties of Ytterbium Oxide (Yb<sub>2</sub>O<sub>3</sub>) (2019). Honors Undergraduate Theses. 641. University of Central Florida, Orlando, United States, <https://stars.library.ucf.edu/honorsthesis/641>.
- [4] A. Bhattacharya, R. Srinivasa Rao, M. Ghanashyam Krishna, Characterization of Yb<sub>2</sub>O<sub>3</sub> based optical temperature sensor for high temperature applications, Sensors and Actuators A: Physical 134 (2007) 348-356, <https://doi.org/10.1016/j.sna.2006.05.036>.
- [5] X. Zhu, Y. Zhou, K. Hirao, T. Ishigaki and Y. Sakka, Potential use of only Yb<sub>2</sub>O<sub>3</sub> in producing dense Si<sub>3</sub>N<sub>4</sub> ceramics with high thermal conductivity by gas pressure sintering, Sci. Technol. Adv. Mater. 11 (2010) 065001, <https://doi.org/10.1088/1468-6996/11/6/065001>.
- [6] Y. Cui, R. Shi, J. Liu, H. Wang, H. Li, Yb<sub>2</sub>O<sub>3</sub> Doped Zr<sub>0.92</sub>Y<sub>0.08</sub>O<sub>2-α</sub>(8YSZ) and Its Composite Electrolyte for Intermediate Temperature Solid Oxide Fuel Cells, Materials 11 (2018), 1824, <https://doi.org/10.3390/ma11101824>.
- [7] J. Bu, Y. Gu, M. Chen, Y. Chen and Z. Wang, Effect of Nano-Yb<sub>2</sub>O<sub>3</sub> addition on crystallization and sintering properties of fused quartz ceramic materials, J. Ceram. Soc. of Japan 121 (2013) 968-971, <https://doi.org/10.2109/jcersj2.121.968>.
- [8] Y. Zheng, Emission behaviors of Yb<sub>2</sub>O<sub>3</sub> nanoparticles pumped by 980 nm laser at different power densities, Opt. Laser Technol. 63 (2014) 39-44, <https://doi.org/10.1016/j.optlastec.2014.03.012>.
- [9] A. A. Ibrahim, R. Ahmadd, A. Umara, M.S. Al-Assirib, e, A.E. Al-Salamif, R. Kumarg, S.G. Ansari, S. Baskoutas, Two-dimensional ytterbium oxide nanodisks based biosensor for selective detection of urea, Biosensors and Bioelectronics 98 (2017) 254-260, <http://dx.doi.org/10.1016/j.bios.2017.06.015>.
- [10] S. Chaudhary, S. Kumar, G. R. Chaudhary, Tuning of structural, optical and toxicological properties of Gd<sup>3+</sup> doped Yb<sub>2</sub>O<sub>3</sub> nanoparticles, Ceram. Int. 45 (2019) 19307–19315, <https://doi.org/10.1016/j.ceramint.2019.06.181>.

- [11] M. S. Henriques, A. C. Ferreira, A. Cruz, L. M. Ferreira, J. B. Branco, P. Brázda, K. Jurek, T. Stora, A.P.Gonçalves, Preparation of Yb<sub>2</sub>O<sub>3</sub> submicron-and nano-materials via electrospinning, *Ceram. Int.* 41 (2015) 10795-10802, <http://dx.doi.org/10.1016/j.ceramint.2015.05.017>.
- [12] Y. Sohn, Yb<sub>2</sub>O<sub>3</sub> nanowires, nanorods and nano-square plates, *Ceram. Int.* 44 (2018) 3341-3347, <https://doi.org/10.1016/j.ceramint.2017.11.118>.
- [13] D. P. Rojas, L. Fernández Barquín, J. I. Espeso, J. Rodríguez Fernández and J. Chaboy, Reduction of the Yb valence in YbAl<sub>3</sub> nanoparticles, *Phys. Rev B* 78 (2008) 094412, <https://doi.org/10.1103/PhysRevB.78.094412>.
- [14] D. P. Rojas, L. Fernández Barquín, J.I. Espeso, J. Rodríguez Fernández, D. Alba Venero, J.A. Gallastegui, G.R. Castro, V. A. Ivanshin, Coexistence of ferromagnetism and spin glass state in YbNi<sub>2</sub> nanoparticles, *J. Magn. Magn Matter* 475 (2019) 264-270, <https://doi.org/10.1016/j.jmmm.2018.11.123>.
- [15] D. P. Rojas, L. Fernández Barquín, J. Rodríguez Fernández, J. I. Espeso, J. C. Gómez Sal, Size effects in the magnetic behaviour of TbAl<sub>2</sub> milled alloys, *J. Phys: Condens. Matter* 19 (2007) 186214, <https://doi.org/10.1088/0953-8984/19/18/186214>.
- [16] E. M. Jefremovas, M. de la Fuente Rodríguez, J. Alonso, J. Rodríguez Fernández 1, J. I. Espeso, I. Puente-Orench, D. P. Rojas, A. García-Prieto, M. L. Fdez-Gubieda, L. Rodríguez Fernández, and L. Fernández Barquín, Exploring the Different Degrees of Magnetic Disorder in Tb<sub>x</sub>R<sub>1-x</sub>Cu<sub>2</sub> Nanoparticle Alloys, *Nanomaterials* 10 (2020) 2148, <https://doi.org/10.3390/nano10112148>.
- [17] J. Rodríguez-Carvajal, Recent advances in magnetic structure determination by neutron powder diffraction, *Physica B* 192 (1993) 55. For recent versions and details consult the site: <https://www.ill.eu/sites/fullprof/>
- [18] Transmission Electron Microscopy Characterization of Nanomaterials, edited by Challa S.S.R. Kumar (Springer, Berlin, Heidelberg, 2014), <https://doi.org/10.1007/978-3-642-38934-4>.
- [19] D. P. Rojas, L. Fernández Barquín, J Rodríguez Fernández, L Rodríguez Fernández and J. Gonzalez, Phonon softening on the specific heat of nanocrystalline metals, *Nanotechnology* 21 (2010) 445702, <http://dx.doi.org/10.1088/0957-4484/21/44/445702>.
- [20] D. P. Rojas, L. Fernández Barquín, J Rodríguez Fernández, J. I.Espeso and J. C. Gómez Sal, Magnetization and specific heat of nanocrystalline rare-earth TbAl<sub>2</sub>, TbCu<sub>2</sub> and GdAl<sub>2</sub> alloys, *J. Phys: Conf. Ser.* 200 (2010) 072080, <https://doi.org/10.1088/1742-6596/200/7/072080>.

- [21] D. P. Rojas, L. Fernández Barquín, J. Sánchez Marcos, C. Echevarria-Bonet, J. I. Espeso, J. Rodríguez Fernández, L. Rodríguez Fernández and M. H. Mathon, Magnetic disorder in TbAl<sub>2</sub> nanoparticles, Mater. Res. Express 2 (2015) 075001, <https://doi.org/10.1088/2053-1591/2/7/075001>.
- [22] B. H. Justice, E. F. Westrum Jr., Thermophysical Properties of the Lanthanide Oxides. Ii. Heat Capacities, Thermodynamic Properties, and Some Energy Levels of Samarium (iii), Gadolinium (iii), and Ytterbium (iii) Oxides from 10 to 350° K, J. Phys. Chem 67 (1963) 345-351, <https://doi.org/10.1021/j100796a032>.
- [23] R. M. Moon, W. C. Koehler, H. R. Child, and L. J. Raubenheimer, Magnetic Structures of Er<sub>2</sub>O<sub>3</sub> and Yb<sub>2</sub>O<sub>3</sub>, Phys. Rev. 176 (1968) 722, <https://link.aps.org/doi/10.1103/PhysRev.176.722>.
- [24] C. Echevarria-Bonet, D. P. Rojas, J. I. Espeso, J. Rodríguez Fernández, L. Rodríguez Fernández, E. Bauer, S. Burdín, S. G. Magalhães, and L. Fernández Barquín, Breakdown of the coherence effects and Fermi liquid behavior in YbAl<sub>3</sub> nanoparticles, J. Phys: Cond. Matter 30 (2018) 135604, <https://doi.org/10.1088/1361-648X/aab0c7>.
- [25] J. B. Gruber, R. D. Chirico and E. F. Westrum Jr., Correlation of spectral and heat-capacity Schottky contributions for Dy<sub>2</sub>O<sub>3</sub>, Er<sub>2</sub>O<sub>3</sub>, and Yb<sub>2</sub>O<sub>3</sub>, J. Chem. Phys. 76 (1982) 4600-4605, <https://doi.org/10.1063/1.443538>.
- [26] K. R. Lea, M. J. M. Leask and W. P. Wolf, The raising of angular momentum degeneracy of *f*-electron terms by cubic crystal fields, J. Phys. Chem. Solids 23 (1962) 1381-1405, [https://doi.org/10.1016/0022-3697\(62\)90192-0](https://doi.org/10.1016/0022-3697(62)90192-0).
- [27] E. S. R. Gopal, Specific Heats at Low Temperatures (New York: Plenum Press, 1966).
- [28] B. R. Powell Jr., O. Hunter Jr., W. R. Manning, Elastic Properties of Polycrystalline Ytterbium Oxide, J. Amer. Ceram. Soc. 54 (1971) 488, <https://doi.org/10.1111/j.1151-2916.1971.tb12185.x>.
- [29] S. D. Pandey, K. Samanta, J. Singh, N. D. Sharma and A. K. Bandyopadhyay, Anharmonic behavior and structural phase transition in Yb<sub>2</sub>O<sub>3</sub>, AIP Adv.3 (2013) 122123, <https://doi.org/10.1063/1.4858421>.
- [30] Y. U. Jinqui, C. Lei, H.E. Huaqiang, Y. Shihong, H.U. Yunsheng, W.U. Hao, Raman spectra of RE<sub>2</sub>O<sub>3</sub> (RE=Eu, Gd, Dy, Ho, Er, Tm, Yb, Lu, Sc and Y): laser-excited luminescence and trace impurity analysis, J. Rare Earths 32 (1) (2014) 1, [https://doi.org/10.1016/S1002-0721\(14\)60025-9](https://doi.org/10.1016/S1002-0721(14)60025-9).
- [31] M. V. Abrashev, N. D. Todorov, and J. Geshev, Raman spectra of R<sub>2</sub>O<sub>3</sub> (R-Rare earth) sesquioxides with C-type bixbyite crystal structure: A comparative study, J. Appl. Phys. 116, (2014) 103508, <https://doi.org/10.1063/1.4894775>.

- [32] D. C. Wallace, *Thermodynamics of Crystals* (New York: Wiley, 1972)
- [33] C. A. Martin, Simple treatment of anharmonic effects on the specific heat, *J. Phys.: Condens. Matter* 3 (1991) 5967, <https://doi.org/10.1088/0953-8984/3/32/005>.
- [34] J. I. Facio, D. Betancourth, N. R. Cejas Bolecek, G. A. Jorge, P. Pedrazzini, V. F. Correa, P. S. Cornaglia, V. Vildosola, D. J. García, Lattice specific heat for the RMIn<sub>5</sub> (R=Gd, La, Y; M=Co, Rh) compounds: Non-magnetic contribution subtraction, *J. Magn Magn Matter* 407 (2016) 406, <http://dx.doi.org/10.1016/j.jmmm.2016.01.053>.
- [35] A. K. Arora, M. Rajalakshmi, T. R. Ravindran, Phonon Confinement in Nanostructured Materials, *Encyclopedia of Nanoscience and Nanotechnology* Edited by H. S. Nalwa Vol. 8 (American Scientific Publishers, 2004). pags 499–512.
- [36] Rosa Martín-Rodríguez, *Synthesis, structural characterization and spectroscopic study of nanocrystalline and microcrystalline materials* (2010). PhD Thesis. University of Cantabria, Santander, Spain, <https://repositorio.unican.es/xmlui/handle/10902/1564>.
- [37] X. Yan, X. Ren, D. He, B. Chen, W. Yang, Mechanical behaviors and phase transition of Ho<sub>2</sub>O<sub>3</sub> nanocrystals under high pressure, *J. Appl. Phys* 116 (2014) 033507, <http://dx.doi.org/10.1063/1.4890341>.
- [38] A. Kumar, V. Mishra, M. Kamal Warshi, A. Sati1, A. Sagdeo, R. Kumar, P. R. Sagdeo, Strain induced disordered phonon modes in Cr doped PrFeO<sub>3</sub>, *J. Phys: Cond. Matter* 31 (2019) 275602, <https://doi.org/10.1088/1361-648X/ab1195>.
- [39] M. E. Manley, B. Fultz, L. J. Nagel, Heat capacity and microstructure of ordered and disordered Pd<sub>3</sub>V, *Philos. Mag. B* 80:6 (2000) 1167, <https://doi.org/10.1080/13642810008208589>.

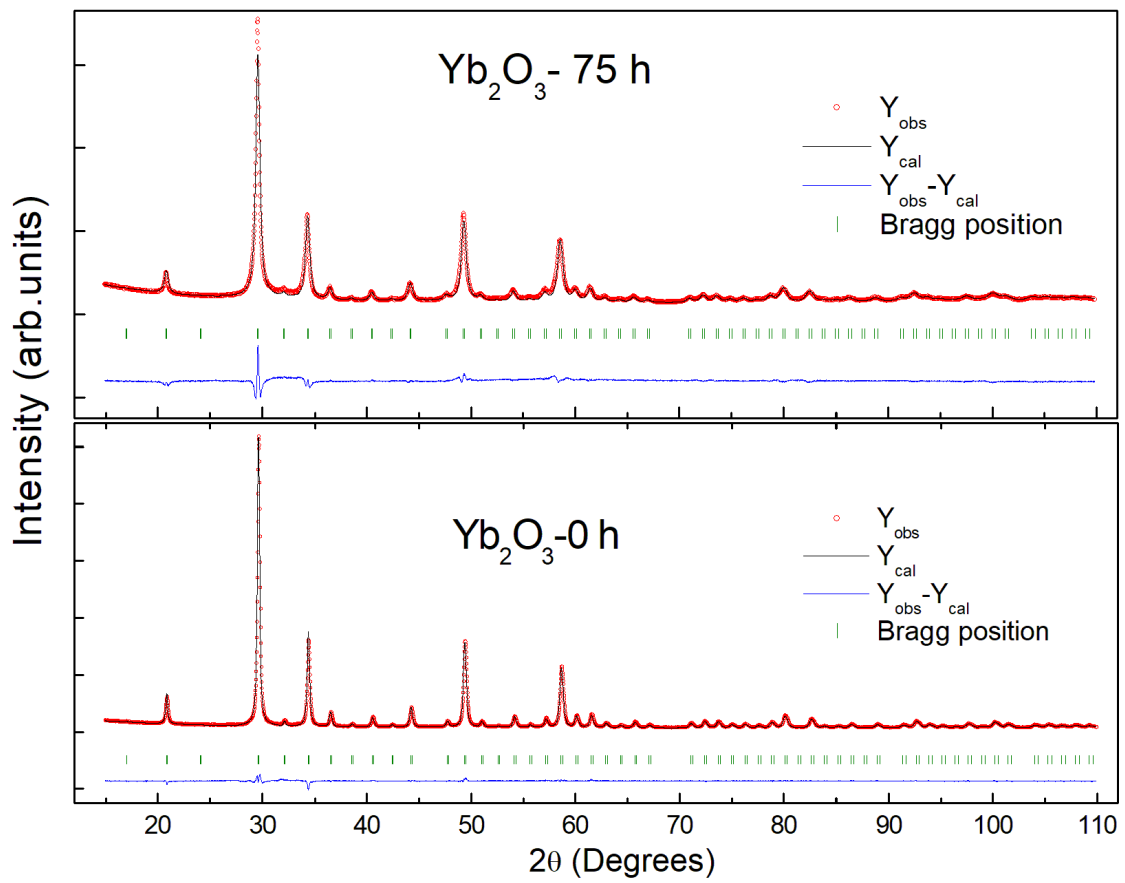


Figure 1. Results of the Rietveld refinements of the X-ray diffraction data in the unmilled (0 h) (bottom) and 75 h milled (top)  $\text{Yb}_2\text{O}_3$  samples. In both cases an excellent reliability of the fitting results is obtained with Bragg factors ( $R_{\text{Bragg}}$ ) below 10 %.

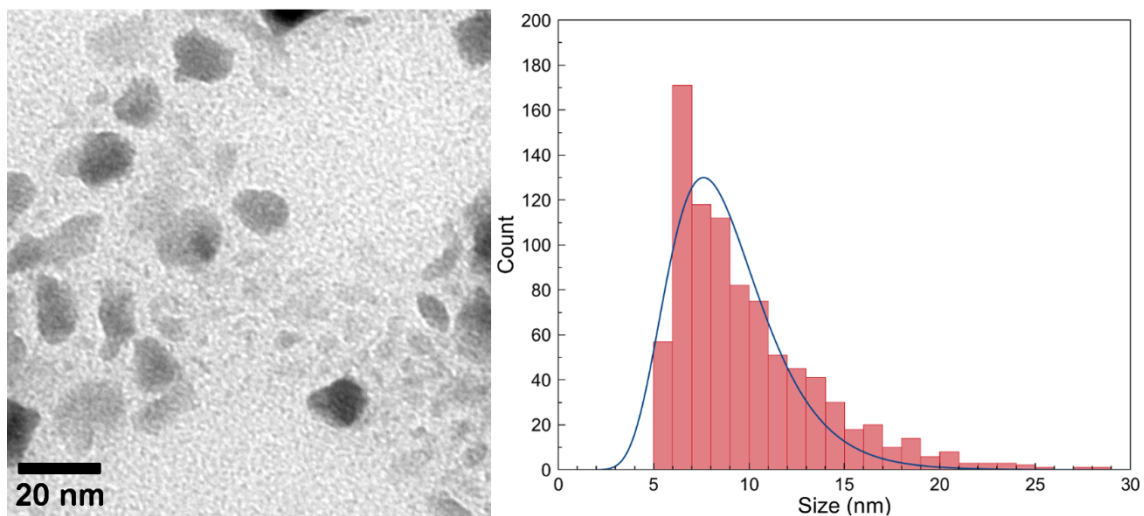


Figure 2. Left: TEM image of representative nanoparticles with a mean size of 8(2) nm of 75 h milled  $\text{Yb}_2\text{O}_3$  sample resulting from the analysis of the histogram distribution of sizes. Right: Histogram of the size distribution and log-normal fit. Milling bulk Ytterbia for 75 hours is enough to produce an ensemble of  $\text{Yb}_2\text{O}_3$  nanoparticles.

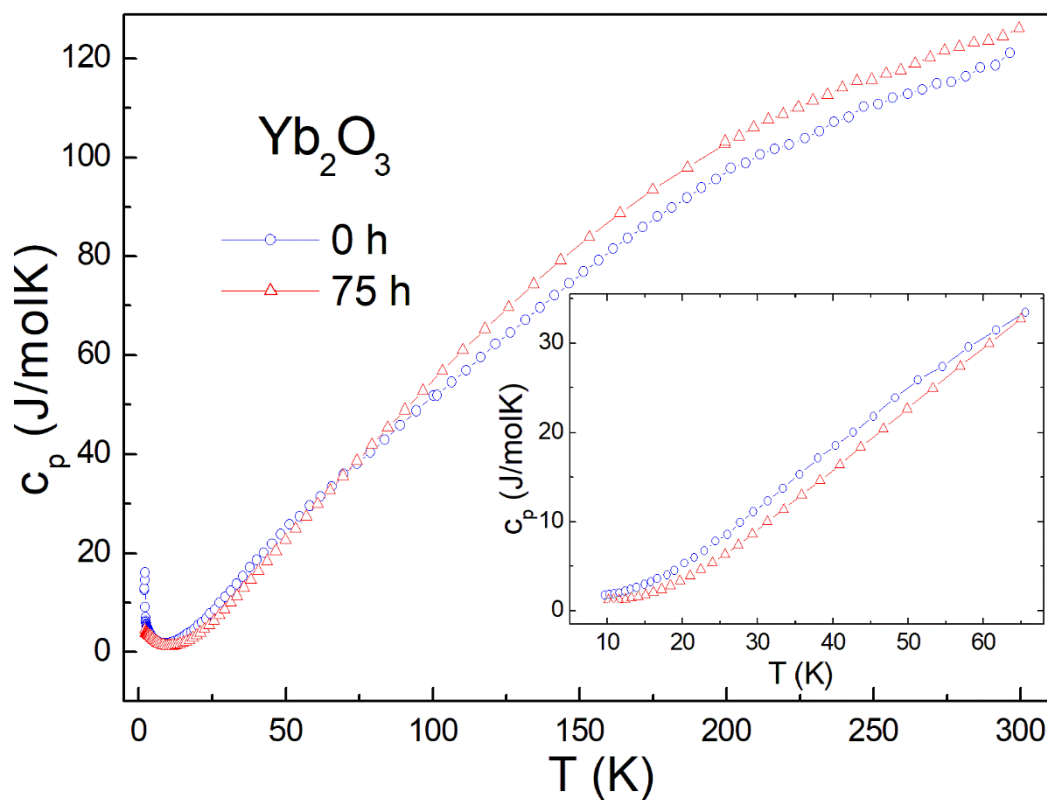


Figure 3. Specific heat at constant pressure vs. temperature curves for the unmilled (0 h) and 75 h milled  $\text{Yb}_2\text{O}_3$  samples. An excess contribution in the milled respect to the unmilled one is observed above 70 K. A detail of the region between 10 K and 70 K is depicted in the inset.

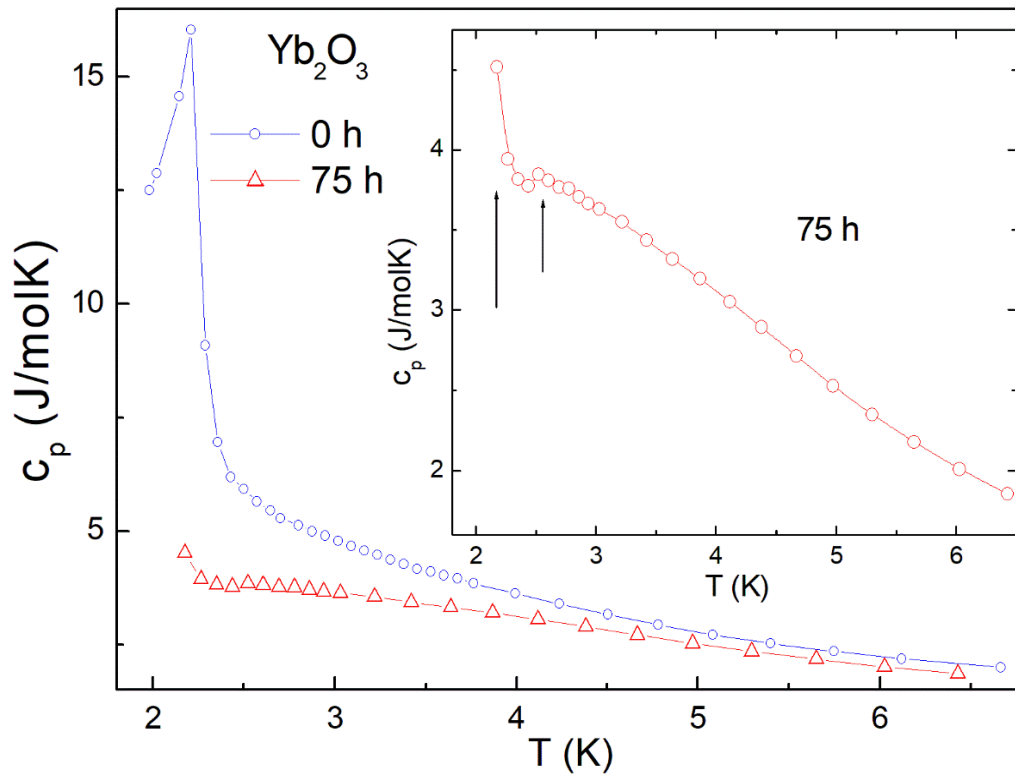


Figure 4. Low temperature region of the specific heat at constant pressure vs. temperature curves for the unmilled (0 h) and 75 h milled  $\text{Yb}_2\text{O}_3$  samples. A drastic change of the peak is observed after the milling process. Details of the double-peaked shape contribution in the 75 h milled sample are depicted in the inset.

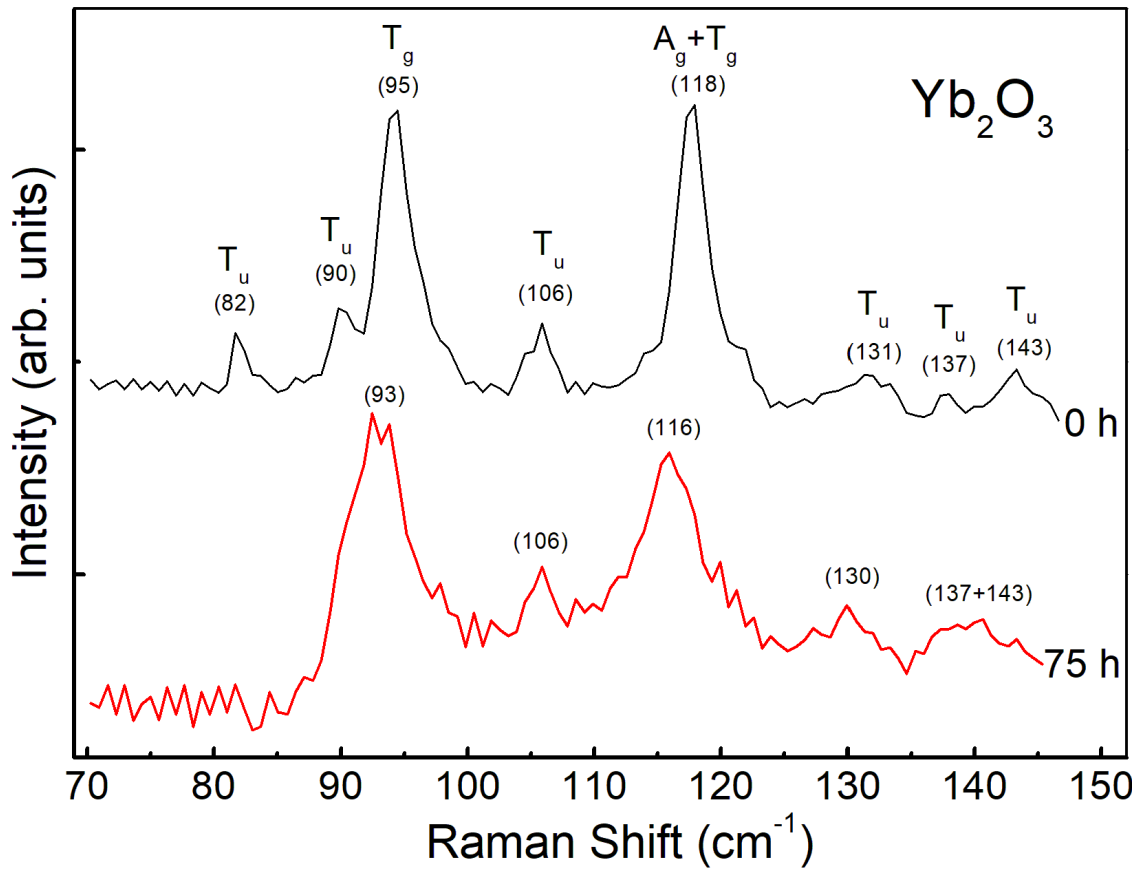


Figure 5. Raman spectra of the un-milled (0 h) and 75 h milled  $\text{Yb}_2\text{O}_3$  oxide at room temperature with mode assignment [25] and indication of the positions of the main contributions in the low frequency region. Broadening (for instance: the two  $T_u$  modes between  $135 \text{ cm}^{-1}$  and  $145 \text{ cm}^{-1}$ ) and shifts of the positions (for instance:  $T_g$  and  $A_g + T_g$  modes) of the 75 h milled respect to the bulk  $\text{Yb}_2\text{O}_3$  oxide are observed.

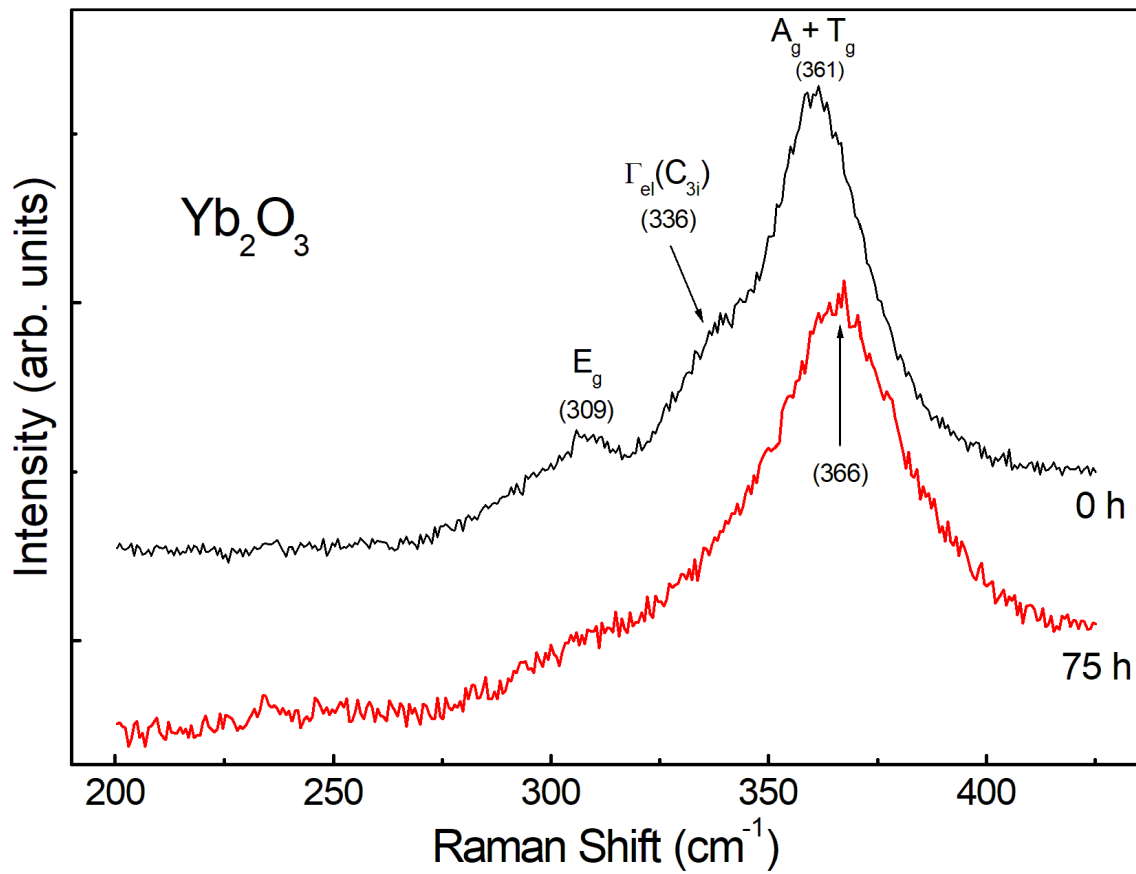


Figure 6. Raman spectra of the unmilled (0 h) and 75 h milled Yb<sub>2</sub>O<sub>3</sub> oxide at room temperature with mode assignment [25] and indication of the positions of the main contributions in the mid-frequency range of the measurements.

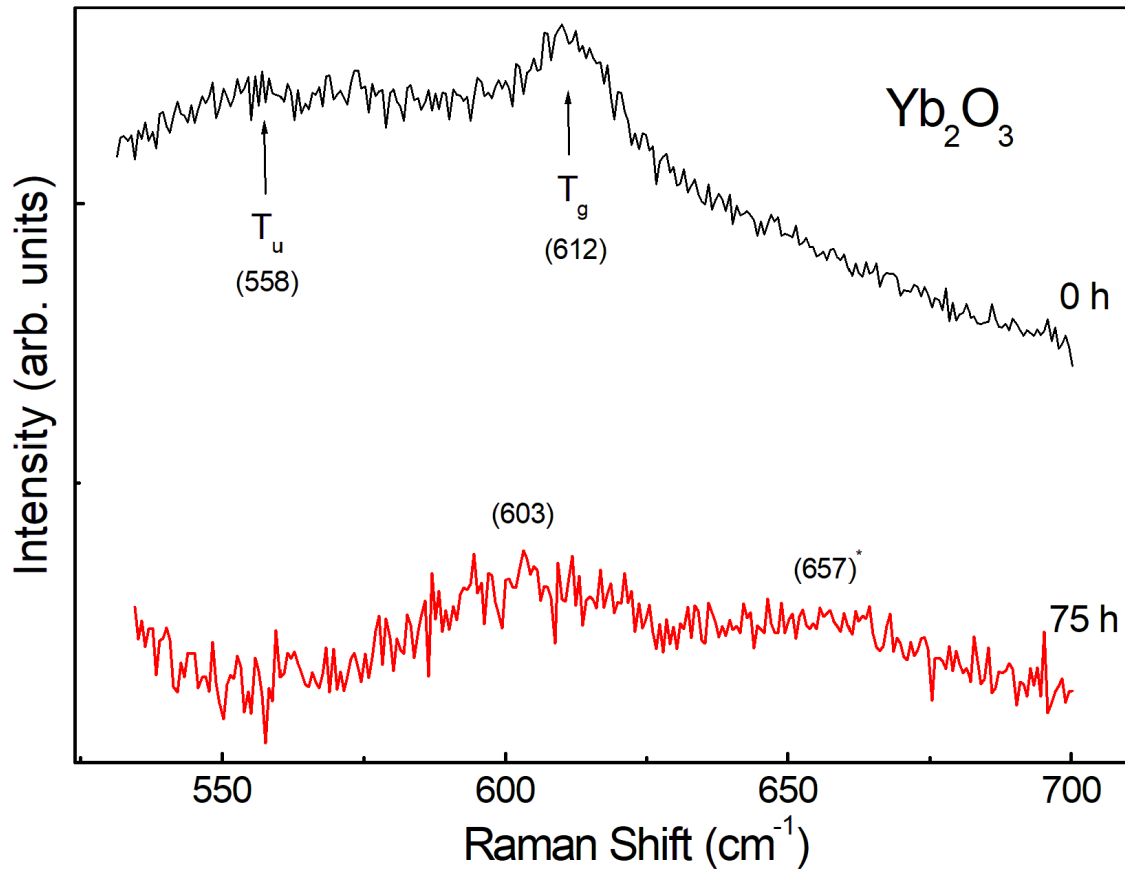


Figure 7. Raman spectra of the unmilled (0 h) and 75 h milled  $\text{Yb}_2\text{O}_3$  oxide at room temperature with mode assignment [25] and indication of the positions of the main contributions in the high frequency region. A new contribution (broad hump) around 657  $\text{cm}^{-1}$  in the 75 h milled respect to the unmilled (0 h)  $\text{Yb}_2\text{O}_3$  is observed.

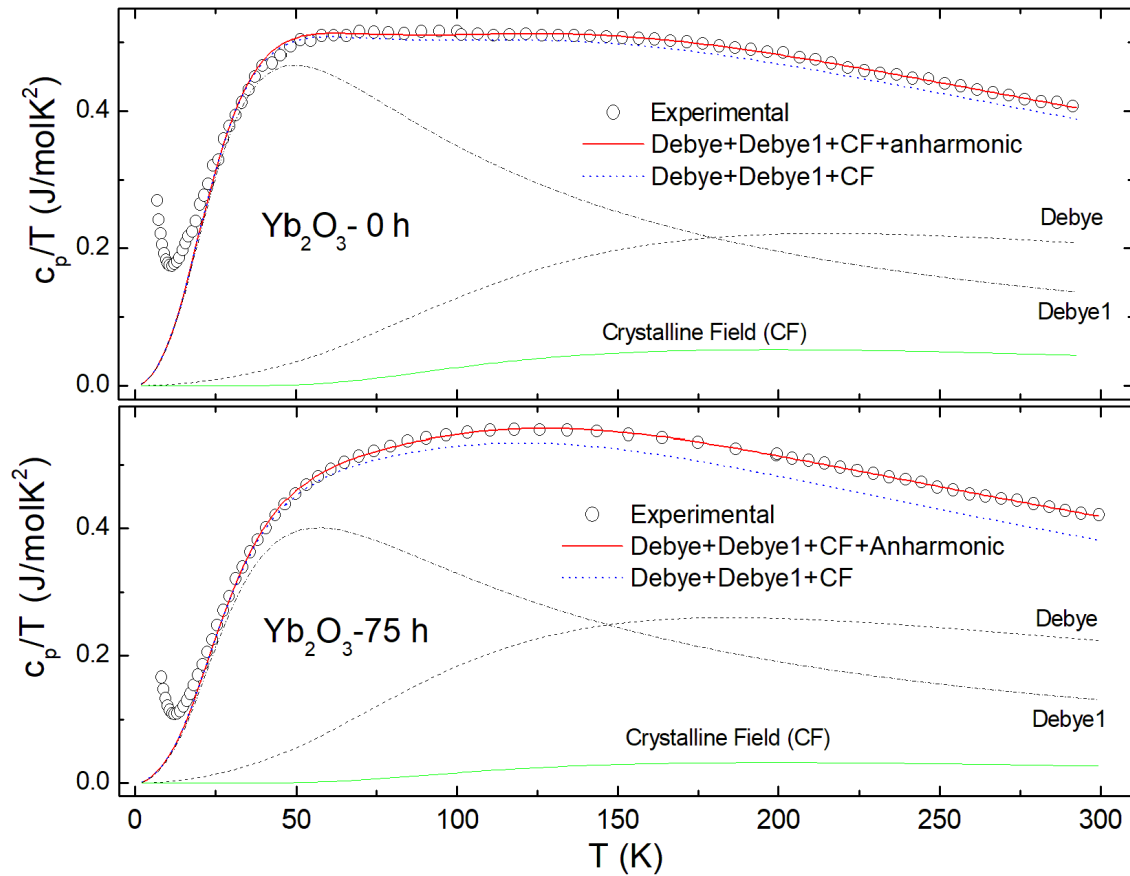


Figure 8-  $c_p/T$  vs. temperature curves for unmilled (0 h) (top) and 75 h milled (bottom)  $\text{Yb}_2\text{O}_3$  oxide. The partial contributions from the crystalline field effects (CF), and two Debye contributions with temperatures Debye ( $\theta_{d1}$ ) and Debye1 ( $\theta_{d2}$ ) (see text) are given. A better fit of the experimental data is reached by considering an additional contribution from anharmonic vibrations of the atoms, which are reinforced in the milled sample.